

Supporting Information

Bulk Ferroelectric Metamaterial with Enhanced Piezoelectric and Biomimetic Mechanical Properties from Additive Manufacturing

Jun Li¹, Fan Yang¹, Yin Long¹, Yutao Dong¹, Yizhan Wang¹, Xudong Wang^{1,*}

¹ Department of Materials Science and Engineering, University of Wisconsin-Madison, WI,
53706, USA

E-mail: xudong.wang@wisc.edu

Table of Content

| | |
|---|-----------|
| Crystallinity calculation of printed PVDF-HFP and PVDF..... | 3 |
| Structural influence on metamaterials piezoelectricity | 4 |
| In-series model printing..... | 7 |
| Adhesion energy calculation..... | 8 |
| Fracture toughness calculation | 9 |
| Supporting Figures..... | 10 |
| Supporting Table..... | 29 |
| Supporting Movies | 30 |
| References | 31 |

Crystallinity calculation of printed PVDF-HFP and PVDF

Differential scanning calorimetry was utilized to estimate the crystallinity of 3D printed PVDF-HFP and PVDF film (**Figure. S1b**). In this study, samples of PVDF-HFP and PVDF are analyzed over the temperature range from 60 to 240 °C. A heating rate of 10 °C/min was used with a nitrogen atmosphere around the sample. DSC were performed on a 24.5 mg PVDF-HFP and a 21.9 mg PVDF sample.

The PVDF-HFP has a melting onset temperature of 85.8 °C and melting peak temperature of 131.2 °C, which are lower than the counterparts of PVDF (121.1 °C and 169.9 °C). By integrating the heat flow peaks, the heats of melting in PVDF-HFP and PVDF are around 0.59 J and 1.38 J, respectively and the standard enthalpy of fusion are 24.1 J g⁻¹ and 63.0 J g⁻¹, respectively. The percent crystallinity X_C of each sample is then determined using the following equation:

$$X_C = \frac{\Delta H_f}{\Delta H_f^*} \quad (\text{S3.1})$$

where ΔH_f is the sample enthalpy of fusion, ΔH_f^* is the heat of fusion of perfectly crystalline PVDF and its copolymer (104.7 J g⁻¹).^{1,2} Therefore, the crystallinity of PVDF-HFP is estimated around 23.4% while the significantly higher crystallinity of PVDF is approximately 60.2 %.

Structural influence on metamaterials piezoelectricity

Optimized thickness of each piezoelectric/conductive layer

The piezoelectric coefficient is given by the equation below:

$$d_{33} = \frac{P_3}{\sigma_3} = \frac{(P_r + \epsilon_0 \chi E_3)}{\sigma_3} \quad (\text{S2.1})$$

where P is the polarization, σ is the stress, P_r is the remnant polarization in ferroelectric materials, ϵ_0 is the vacuum permittivity, E is the poling electric field, and χ is the electric susceptibility. According to equation (1), d_{33} of each individual ferro-layer is invariant to layer thickness when a constant electric field (E) was applied during printing.

However, the effective d_{33} of the whole ferroelectric metamaterial is strongly related to the layer thickness. In printed ferroelectric metamaterials with a fixed height, a thinner ferroelectric/electrode layer allows a larger number of ferro-layers in total. Therefore, a higher effective d_{33} can be achieved as the total polarization (P_{total}) is proportional to the number of layers (n):

$$d = \frac{P_{\text{total}}}{\sigma} = \frac{n P_{\text{indiv}}}{\sigma} \quad (\text{S2.2})$$

where P_{indiv} is the polarization of individual ferro-layer. In addition, thinner ferroelectric layer demands a lower *in situ* poling voltage considering the optimized poling electric field of around 3.5 kV/mm. Therefore, a small layer thickness is preferred in our 3D structure.

Based on this rationale, the thickness in this work was chosen according to our printer's resolution. The normal printing layer limit of our 3D printer is 200 μm . We chose a thickness of $\sim 400 \mu\text{m}$ (2 layers of printing) rather than one layer of printing is: (1) to avoid the short circuit between adjacent electrode layer; and (2) to minimize the heat/electric field effect between adjacent piezoelectric layer.

Optimized proportion of piezoelectric/conductive materials

Regarding the ferroelectric-electrode proportion, 1:1 ratio is optimal. This is because the thickness of each layer needs to be minimized (kept at 400 μm) in order to maximize d_{33} (proportional to the total number of ferroelectric layers). At a fix sample height, increasing either layer's thickness (increasing proportion) would reduce the number of ferroelectric layers, and thus lower d_{33} .

Influence of designed porosity on piezoelectricity

First, the piezoelectric coefficients d of ferroelectric metamaterials are measured by a quasistatic piezometer *via* the relation:

$$d = \frac{Q}{F} \quad (\text{S2.3})$$

where Q is the total charge generated by the metamaterials and F is the force applied by the piezometer. The total charge Q contributed by ferroelectric layers can be expressed as:

$$Q = nQ_{\text{indiv}} = n\rho A = nd' \sigma A = nd' F \quad (\text{S2.4})$$

where n is the layer number, Q_{indiv} is the charge of individual ferroelectric layer, ρ is the charge density of PVDF-HFP/Li-KNN material. A is the active surface area of PVDF-HFP/Li-KNN material that contributes charge (contacting electrodes), σ is the stress applied on PVDF-HFP/Li-KNN material and d' is the material's intrinsic piezoelectric coefficient. It should be noted that the intrinsic piezoelectric coefficient (d') of PVDF-HFP/Li-KNN is a material's property and will not be changed by the macroscopic pores. The active surface area (A) decreases as the porosity increases. The porosity (ϕ) is the proportion of designated open pores in the ferroelectric metamaterials, which is equal to the ratio of hollow area to the total cross-section area (A_{total}) of the metamaterial. The active surface (A) was affected by porosity as:

$$A = (1 - \phi) A_{\text{total}} \quad (\text{S2.5})$$

Meanwhile, the stress (σ) increases linearly following A under a constant applied force (F):

$$\sigma = \frac{F}{A} = \frac{F}{(1 - \phi) A_{\text{total}}} \quad (\text{S2.6})$$

As a result, the active surface area term (A, or. the porosity term) is cancelled out in Q_{indiv} , which is actually independent to the porosity (**Figure. S18a**). Theoretically, the effective piezoelectric coefficient d_{33} of the ferroelectric metamaterials is invariant to the porosity.

However, the voltage output V is dependent on the porosity, as voltage of the ferroelectric metamaterials can be approximated as (ignoring the shape/boundary effect of pore on capacitance):

$$V = V_{\text{indiv}} = \frac{Q_{\text{indiv}}}{C_{\text{indiv}}} = \frac{dFt}{k\epsilon_0 A} \quad (\text{S2.7})$$

where V_{indiv} , C_{indiv} , t are the voltage, capacitance and thickness of each ferroelectric layer, respectively, k is the relative permittivity of PVDF-HFP/Li-KNN and ϵ_0 is the vacuum permittivity. Apparently, as the effective area A is directly related to the porosity, higher voltage will be achieved at a higher porosity (**Figure. S18b**).

In-series model printing

Another multi-layer structure where the ferroelectric slabs were individually sandwiched by thin electrode layers was demonstrated (**Figure S13a**), forming an in-series connection of all piezoelectric units, as illustrated by the equivalent circuit in the inset of **Figure S13a**. In order to achieve effective poling during the printing, when processing the Nth piezoelectric unit, all previously printed electrodes were connected and grounded by a conductive bus. Therefore, a high potential drop between nozzle tip (1.4 kV) and the electrode layer (0 V) will produce a strong and concentrated electric field (3.5 kV/mm) to rapidly align the dipoles of extruded ferroelectric materials (**Figure S13b**). Therefore, both temperature and electric field would have minimal influences to the as-printed and aligned piezoelectric units. After printing, the conductive bus was removed to isolate the intercalated electrodes (**Figure S13c**) and achieve in-series connection of all piezoelectric slabs.

This measurement revealed that the total piezoelectric output was contributed by each individual unit adding up together, as a result of the in-series connection. The close voltage output from each unit also evidenced the uniform strain distribution among each piezoelectric slabs as predicted by the simulation. The raise of overall voltage also reflected the capacitance drop due to the in-series connection. As more piezoelectric units were integrated, the overall capacitance dropped from approximately 143 pF at 1 unit to 31 pF at 7 units (**Figure S13d**). Given the capacitance of ambient air (~ 20 pF) and printing flaws, this result matched the in-series connection model well.

To demonstrate the flexible output design capability of this technology, the output voltage and current were measured as a function of printing units under the same mechanical stimuli (**Figure S13e**). The voltage increased monotonously from 7.75 V to 29.36 V, yet not fully linearly. This nonlinearity was primarily due to the small charge loss at the in-between electrodes as a result of their relatively high electrical resistivity compared to metals. The interlayer charge loss could be evidenced by the minute decrease of output current, which slightly dropped from 3.0 μ A to 2.5 μ A. The piezoelectric charge coefficients, d_{33} shared a similar trend as current output, which moderately decreased from 14.76 pC/N (1 unit) to 10.87 pC/N (7 units), as shown in **Figure S13f**. Overall, this design of as-printed 3D structure effectively boosted the voltage response while keeping a relatively stable current output and d_{33} coefficient. This configuration would be particularly useful for voltage sensitive applications with a significantly improved piezoelectric voltage response to applied mechanical stimuli.

Adhesion energy calculation

The relationship of mechanical work by the gripper, adhesion energy of bilayers, and the strain energy related to bilayer bending can be expressed as:

$$F\Delta y = E_{ad}(d\Delta s) + \Delta U \quad (\text{S4.1})$$

where F is the measured force, Δy is the displacement of gripper, E_{ad} is the specific adhesion energy (J m^{-2} or N m^{-1}), d is the width of the printed bilayer, Δs is the interface separation distance, and ΔU is the strain energy due to bending of thin layer.^{3, 4} Therefore, the adhesion energy could be obtained as:

$$E_{ad} = \frac{F}{d} \left(\frac{\Delta y}{\Delta s} \right) - \frac{\Delta U}{d\Delta s} \quad (\text{S4.2})$$

The contribution of bending strain energy is trivial considering the thin thickness of each layer, and therefore it could be neglected ($\Delta U/d\Delta s = 0$). Given the geometry of setup, the gripper displacement Δy is two times as the interface separation distance Δs , ($\Delta y/\Delta s = 2$). The interfacial adhesion energy could be simplified as:

$$E_{ad} = \frac{2F}{d} \quad (\text{S4.3})$$

Based on equation S5.3, the specific adhesion energy could be easily obtained when the separation force and print width are known (**Figure. S14**).

Fracture toughness calculation

Analogous to many mineralized biomaterials, our 3D printed ferroelectric structure emulating nacre exhibit a high degree of inelasticity (**Figure. S16**). Single-value linear-elastic parameters based on crack initiation, such as K_{IC} , cannot represent toughening behavior in these structures where the fracture resistance increases with crack extension.^{5, 6} Therefore, nonlinear-elastic fracture mechanics methods considering the contributions from both elastic and inelastic deformation were utilized to evaluate fracture toughness K_J for stable crack propagation, which relates to the J-integral calculation. J values were calculated from the applied load and instantaneous crack length, which was based on elastic J_{el} and plastic J_{pl} contributions as following:

$$J = J_{el} + J_{pl} \quad (\text{S5.1})$$

The J_{el} based on linear elastic fracture mechanics could be expressed as:

$$J_{el} = \frac{K^2}{E'} \quad (\text{S5.2})$$

where K is the stress-intensity factor and E' is Young's modulus appropriate to plane strain. K and E' could be expressed as following⁷:

$$K = \frac{4P}{B} \sqrt{\frac{\pi}{W}} \left[1.6\left(\frac{a}{W}\right)^{0.5} - 2.6\left(\frac{a}{W}\right)^{1.5} + 12.3\left(\frac{a}{W}\right)^{2.5} - 21.2\left(\frac{a}{W}\right)^{3.5} + 21.8\left(\frac{a}{W}\right)^{4.5} \right] \quad (\text{S5.3})$$

$$E' = \frac{E}{(1-\nu)^2} \quad (\text{S5.4})$$

where P is the maximum applied load in the elastic region, B is the thickness, a is the depth of notch, W is the width, E is young's modulus, and ν is the Poisson's ratio of the sample. The plastic contribution J_{pl} can be calculated by:

$$J_{pl} = \frac{2A_{pl}}{B(W-a)} \quad (\text{S5.5})$$

where the A_{pl} is the plastic area underneath the load-displacement curve. Therefore, the fracture toughness K_J for stable crack propagation could be eventually obtained through the $J-K$ equivalence relationship:

$$K_J = \sqrt{JE'} \quad (\text{S5.6})$$

Supporting Figures

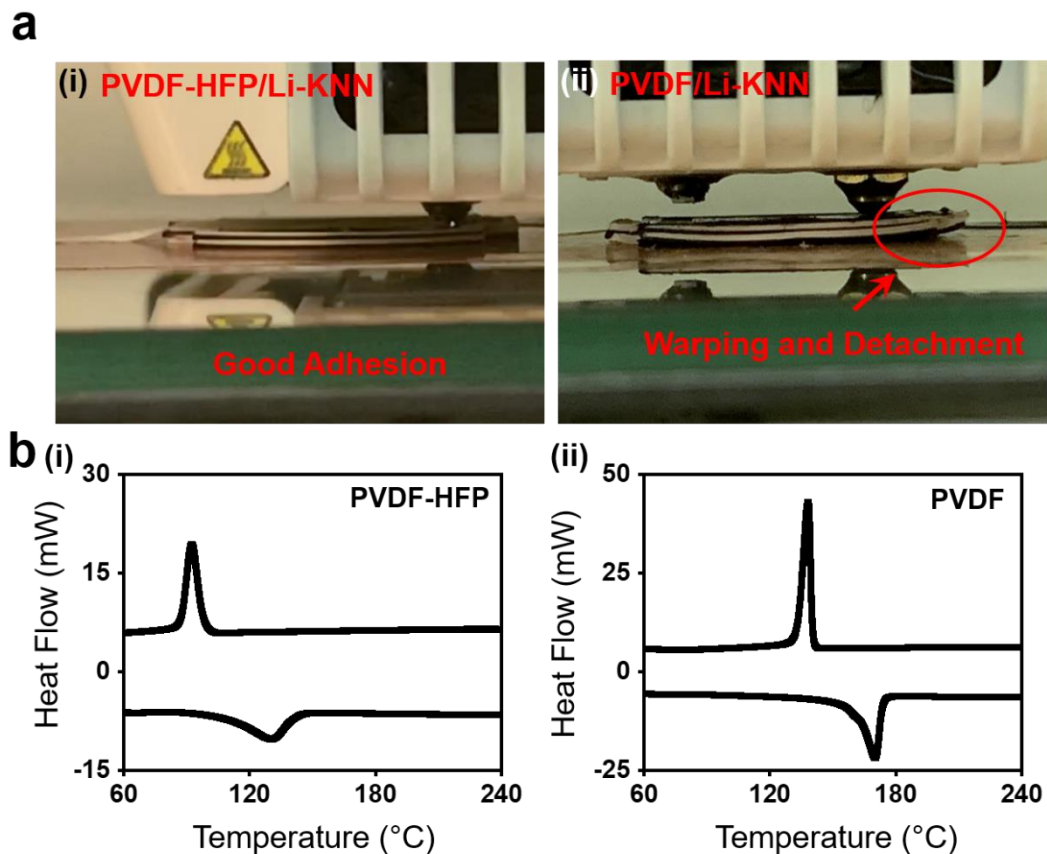


Figure S1. Advantages of PVDF-HFP over PVDF. **a,** (i) Printing PVDF-HFP/Li-KNN composite on PLA/CB surface. (ii) Printing PVDF/Li-KNN composite on PLA/CB surface. The PVDF-HFP/Li-KNN has a better printability than PVDF/Li-KNN as it shows a better adhesion between the first layer and printing bed without warping and detachment. **b,** (i) Differential scanning calorimetry (DSC) curve measured from 3D printed PVDF-HFP film. (ii) DSC curve measured from 3D printed PVDF film. The printed PVDF-HFP film not only exhibited a much lower melting point than PVDF film, its crystallinity based on the DSC test is only around 23.4% which is significantly lower than the value 60.2 % of PVDF. The high crystallinity of printed PVDF will build up strain and stress which cause the print deformation and layer detachment.

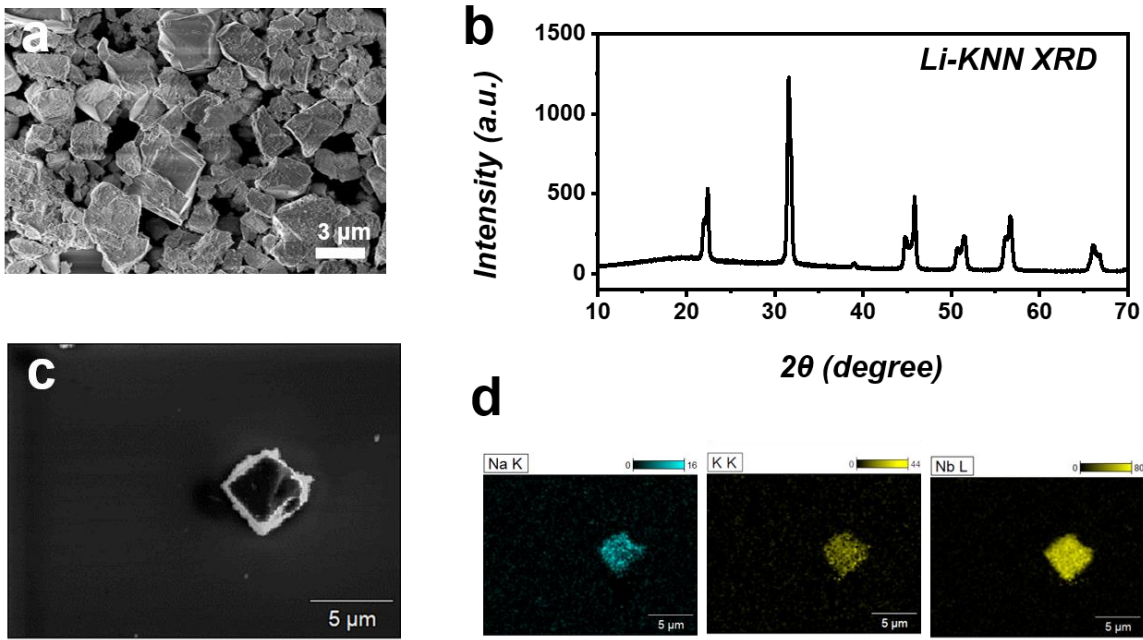


Figure S2. Ferroelectric Li-KNN raw materials. **a**, SEM image of as-synthesized Li-KNN MPs. The MPs have cube-shaped morphology and their size distributed in the range of 2 to 5 μm . **b**, X-ray diffraction pattern of as-synthesized Li-KNN MPs, revealing high crystallinity and no impurity. **c**, SEM image of a single Li-KNN MP. **d**, corresponding EDS mapping of the single MP in c, indicating a uniform distribution of Na, K and Nb elements. The Li element is out of the detection range of EDS mapping.

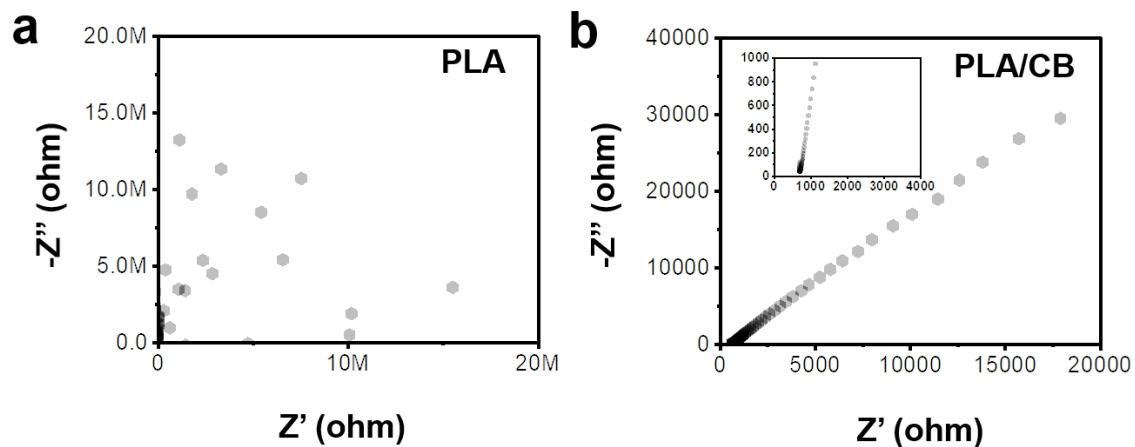


Figure S3. Electrical conductivity of the electrode layer. **a**, Electrochemical impedance spectroscopy (EIS) measurement of pure PLA. The random distribution of data points in PLA measurement suggests its insulating nature. **b**, EIS measurement of PLA/CB composite. The inner resistance of PLA/CB composite could be estimated by the point where the curve intersects with x-axis.

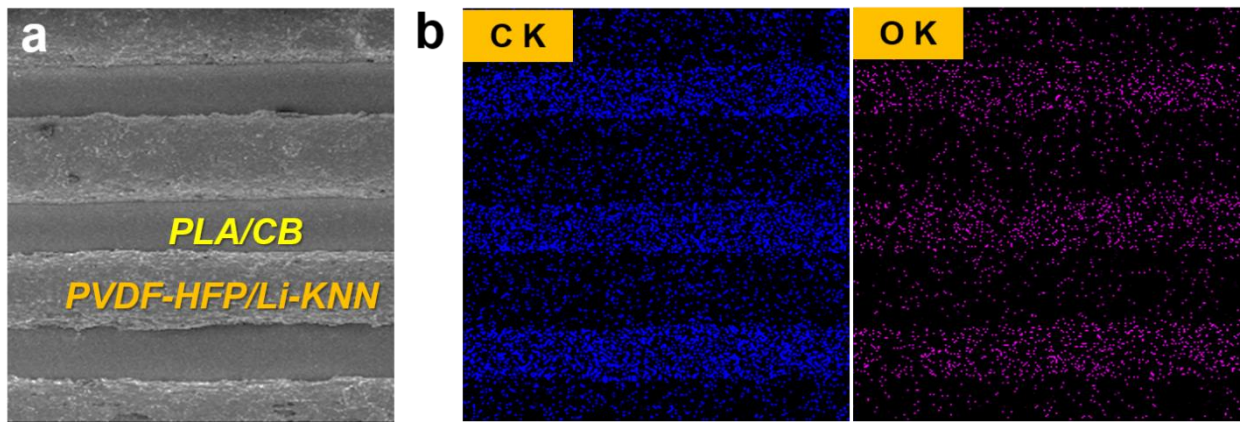


Figure S4. Interface investigation. **a**, SEM image of printed ferroelectric metamaterial. **b**, EDS mapping of C and O elements in the printed structure. Rich C and O elements concentrated on the PLA/CB layer, coinciding with SEM result.

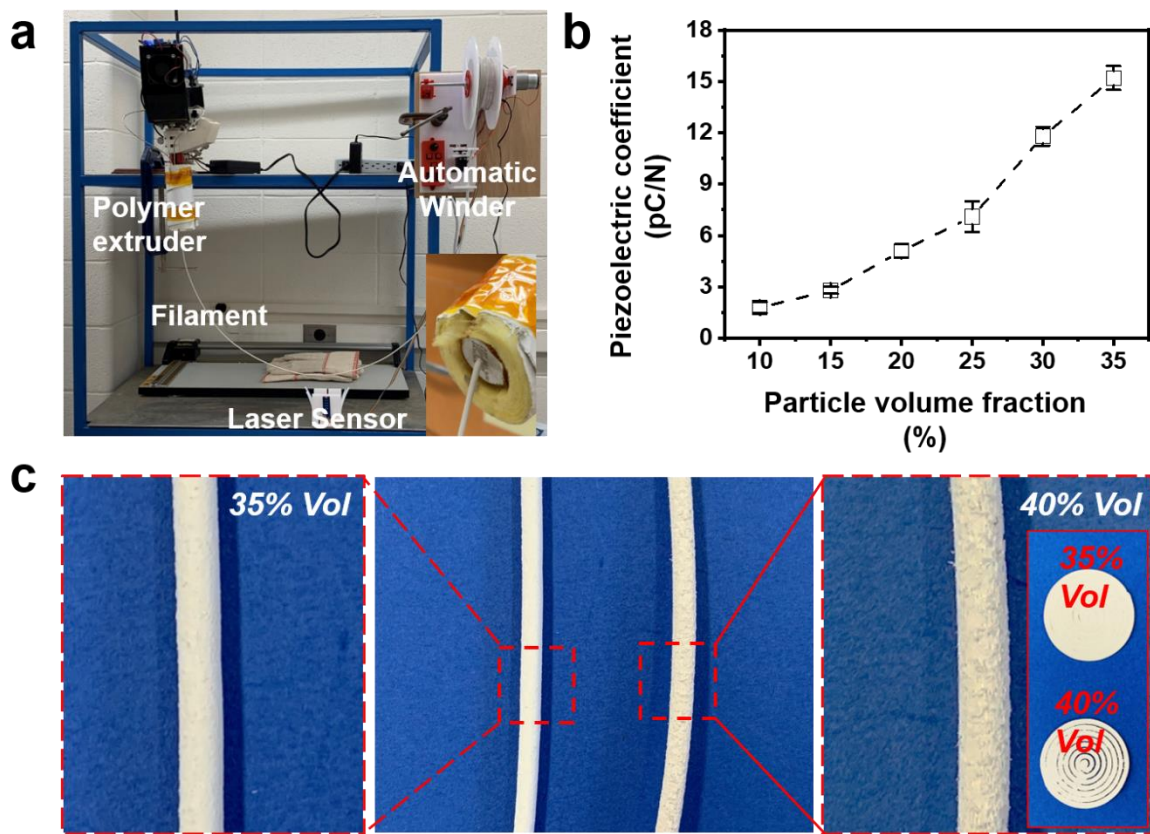


Figure S5. Fabrication and properties of PVDF-HFP/Li-KNN printing raw material. **a**, A customized polymer extrusion system for fabricating composite filaments. Inset is the extrusion of PVDF-HFP/Li-KNN composite filament. **b**, Piezoelectric coefficient d_{33} of printed single ferroelectric layer as a function of particle volume fraction (% vol). The d_{33} coefficient would increase significantly as more particles are blended with PVDF-HFP polymer. **c**, Digital images of comparison of extruded filaments with 35% vol and 40% vol particle loads. The inset is the printed circular disc by utilizing these two filaments. Filament with 35% vol particle load has smoother surface with better printability than filament with 40% vol load.

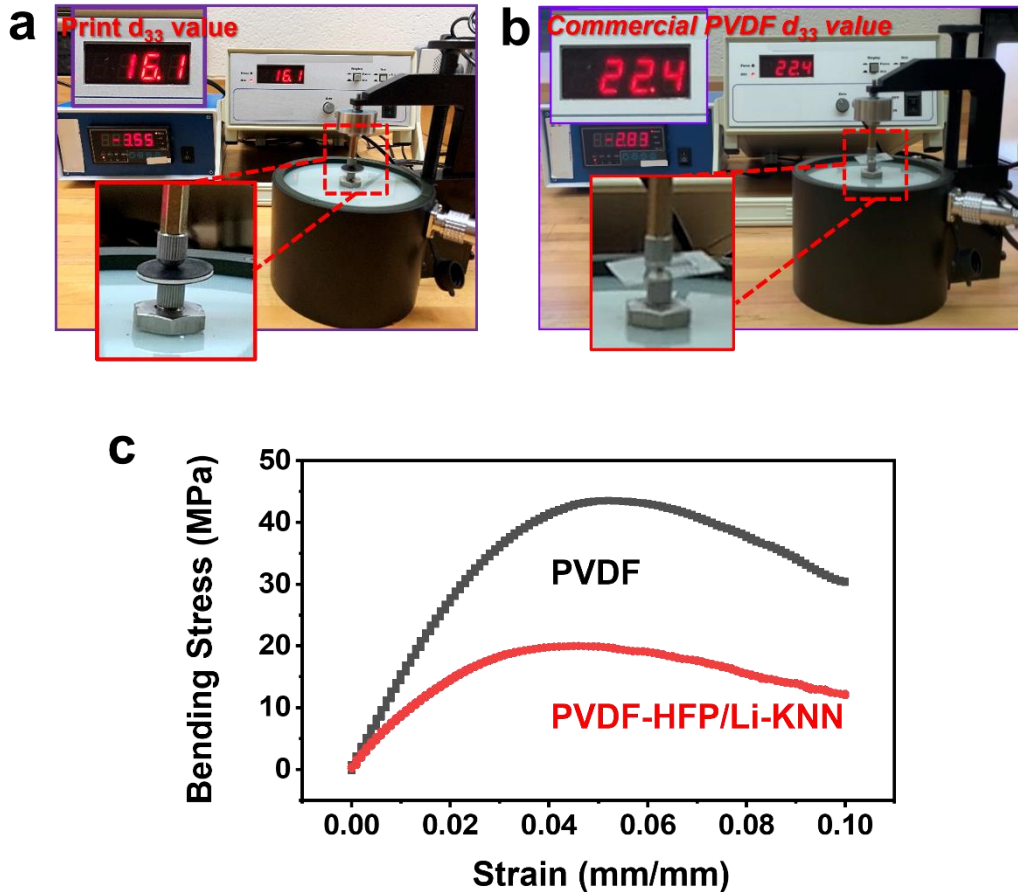


Figure S6. Piezoelectric property of a single ferroelectric layer. **a**, Longitudinal piezoelectric coefficient d_{33} measurement of as-printed single ferroelectric unit based on the Berlincourt method. **b**, Longitudinal piezoelectric coefficient d_{33} measurement of commercial PVDF film. **c**, Flexibility measurement of thick commercial PVDF film ($\sim 500 \mu\text{m}$) and printed PVDF-HFP/Li-KNN film with the same thickness by a three-point bending method.

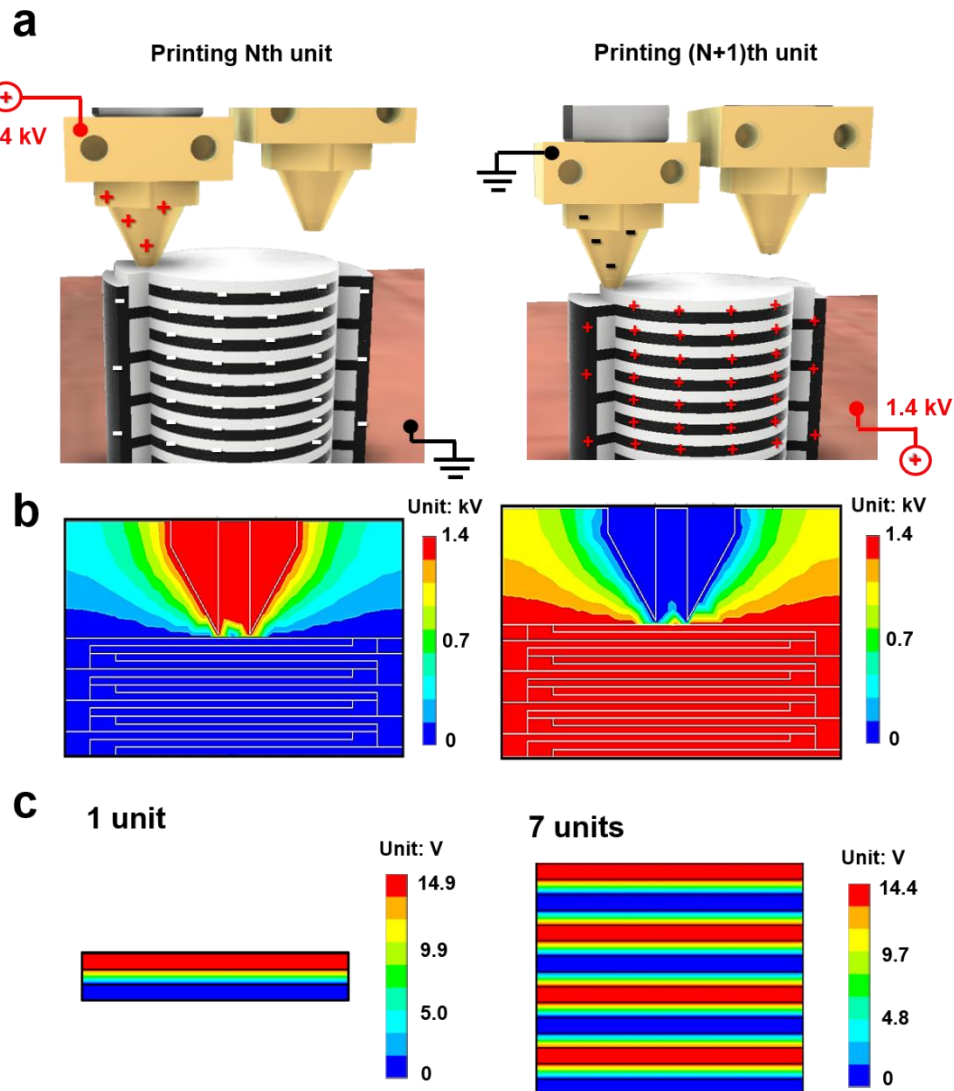


Figure S7. In situ poling electric potential design. **a**, The electrical connection setup for printing ferroelectric metamaterials with interdigital electrode and alternating dipole configuration. The poling voltage (+1.4 kV, 3.5 kV/mm) and ground connections were switched between the nozzle tip and the electrode layers alternatively. **b**, FEA simulation of potential distributions between the printer nozzle and ferroelectric structure. The poling electric field shows the same amplitude but opposite direction. **c**, FEA simulation of potential response of 1-unit structure and 7-unit structure with interdigitated electrode under the same mechanical load. Almost the same voltage outputs were obtained for the two structures.

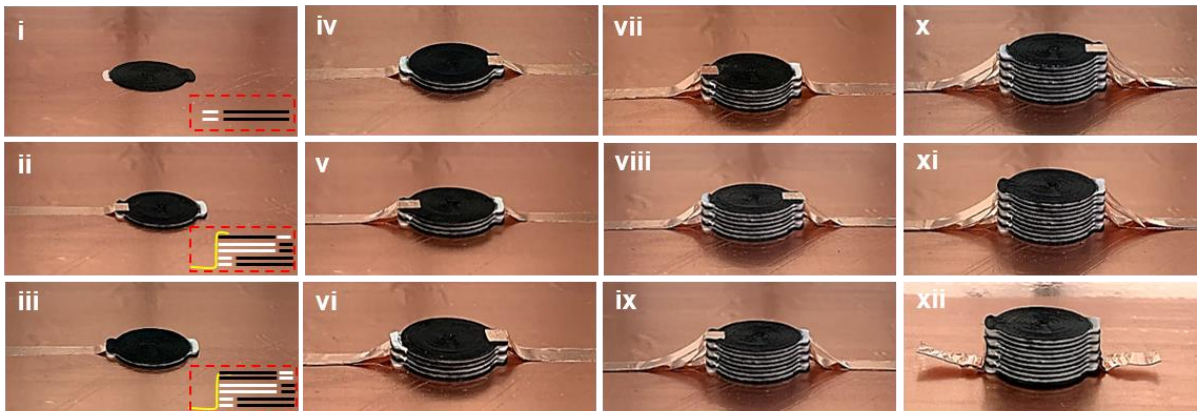
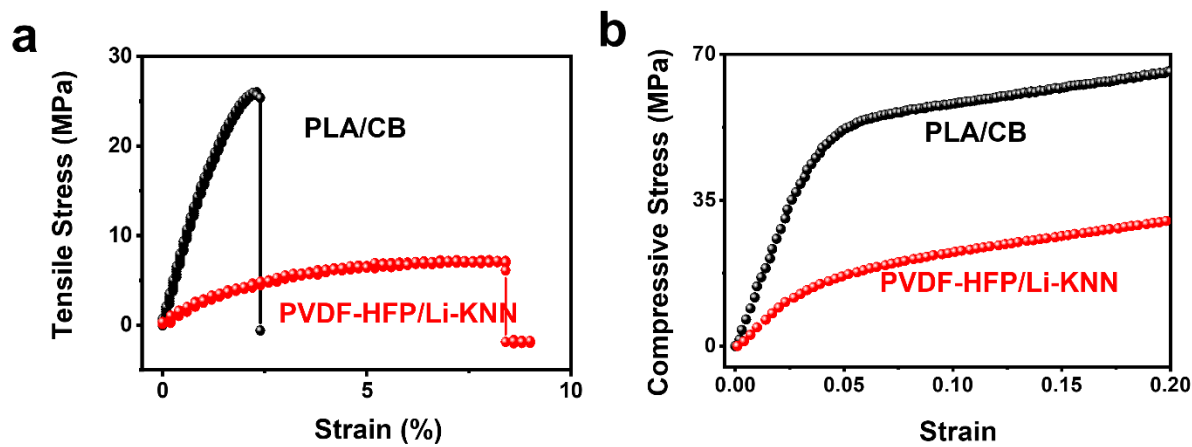
a**Approach 1****b****Approach 2**

Figure S8. Printing process of the multilayered structure. **a**, The printing process under first approach to build the ferroelectric structure by applying two removable copper buses alternatively to the electrode layers. During the ferroelectric layer printing, the electrode layer just below this ferroelectric layer will be connected with printing bed (a glass sheet covered with conductive copper foil). Each ferroelectric or electrode layer consists of two printing layers. The conductive buses are applied between two conductive printing layers as revealed by the schematics in i-iii. **b**, The second approach of building bulk ferroelectric structure by directly printing two buses to connect electrode layers alternatively. This approach allows faster printing and can be scalable. It requires a high position control amount different layers to prevent short circuit of the interdigitated electrodes.



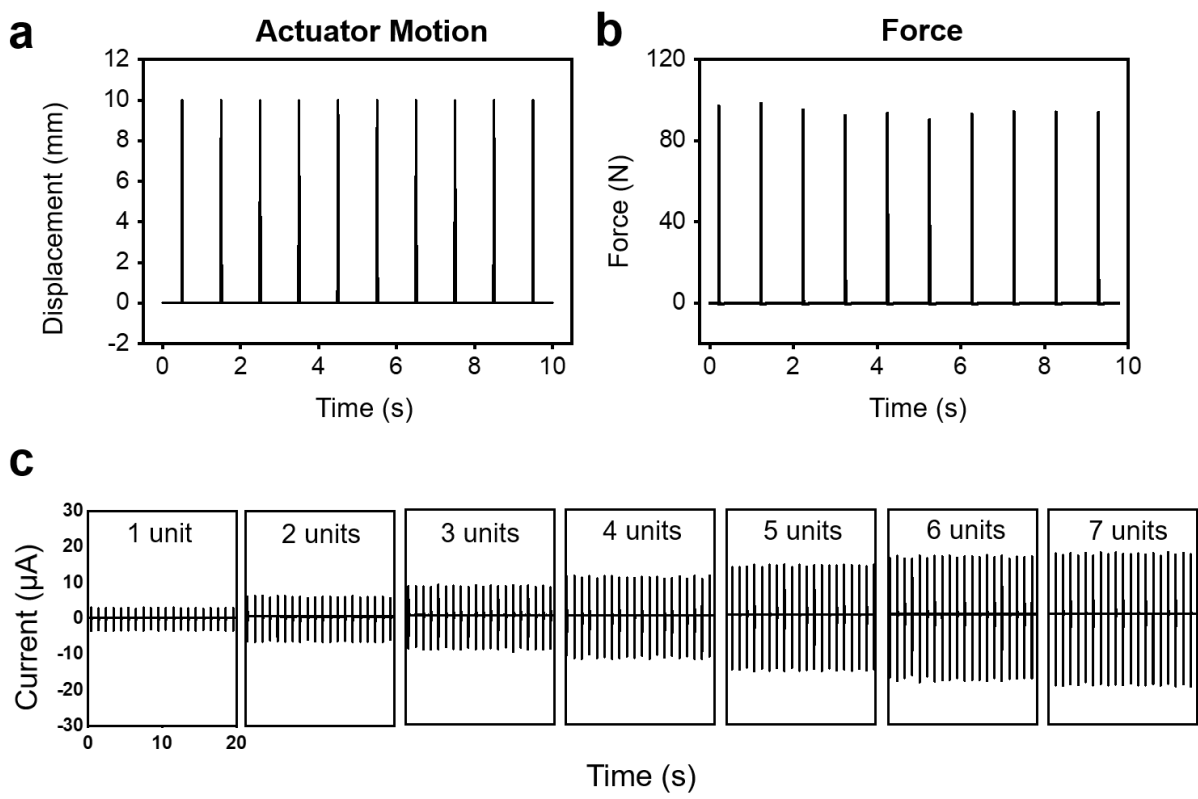


Figure S10. Mechanical stimuli and short circuit data. **a**, The motion curve of computer-controlled actuator that provides constant mechanical stimuli. **b**, The recorded real-time force applied on the ferroelectric print. **c**, Short circuit current outputs of printed structure containing varying ferroelectric units under the same mechanical stimuli applied by the actuator.

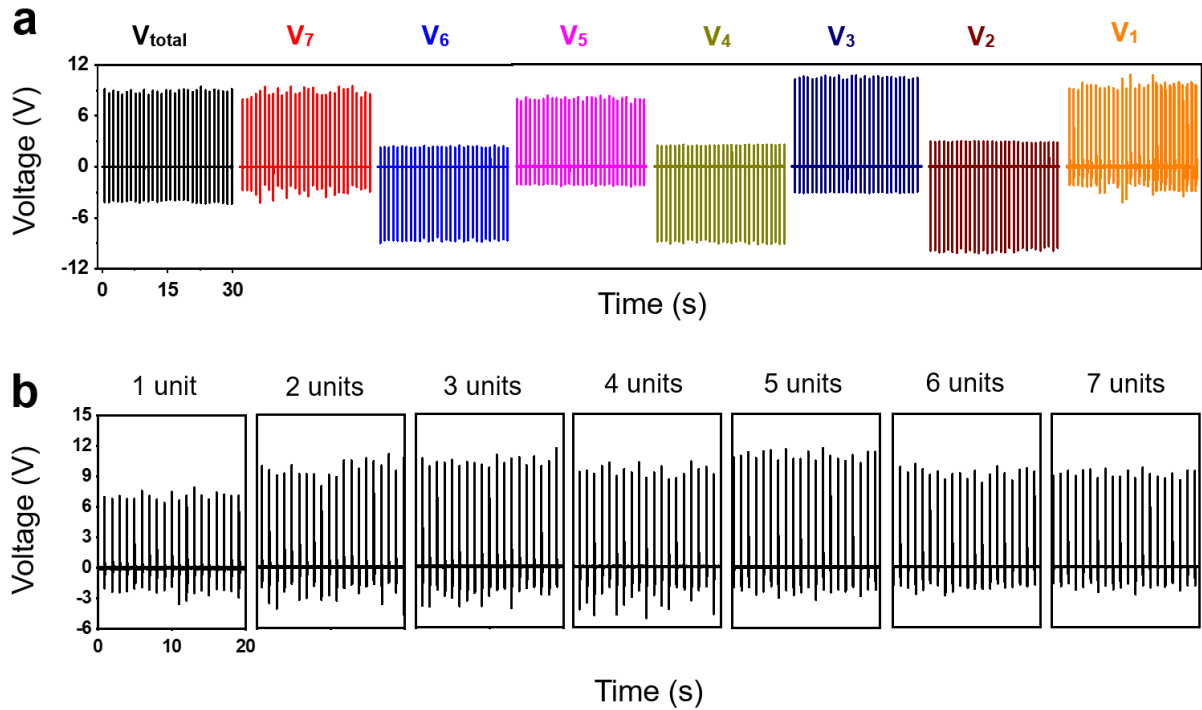


Figure S11. Open circuit voltage measured from metamaterials. **a**, Open-circuited voltage measurement of each ferroelectric layer in the printed seven-unit structure. The amplitudes of voltage outputs of all units are almost the same, indicating similar piezoelectricity in individual unit and a good printability. **b**, Open-circuited voltage outputs of printed structure containing varying ferroelectric units (1 to 7) under the same mechanical stimuli applied by the actuator. The voltage outputs are very close, matching well with previous potential simulation results in Figure. S7c.

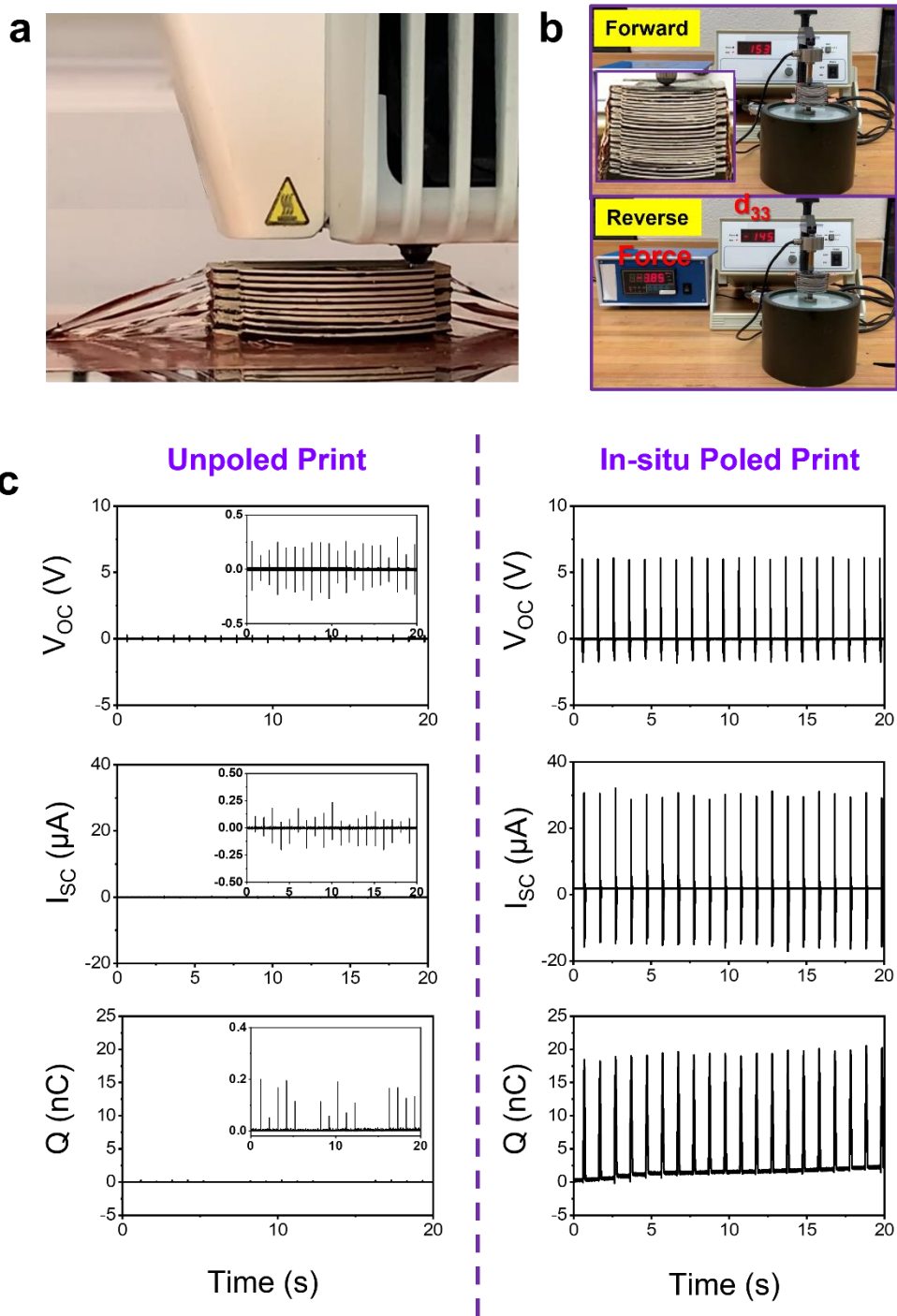


Figure S12. Piezoelectricity of 25-ferro-layered metamaterial. **a**, Digital image of printing of 25-unit bulk structure by utilizing removable buses. **b**, Measurement of the d_{33} coefficient through forward and reverse connections. A close value with different polarity was obtained, which indicates the accurate measurement of real piezoelectricity instead of artifacts. **c**, Comparison of outputs between unpoled printed structure (contributed majorly by triboelectricity) and in-situ poled printed structure (contributed majorly by piezoelectricity).

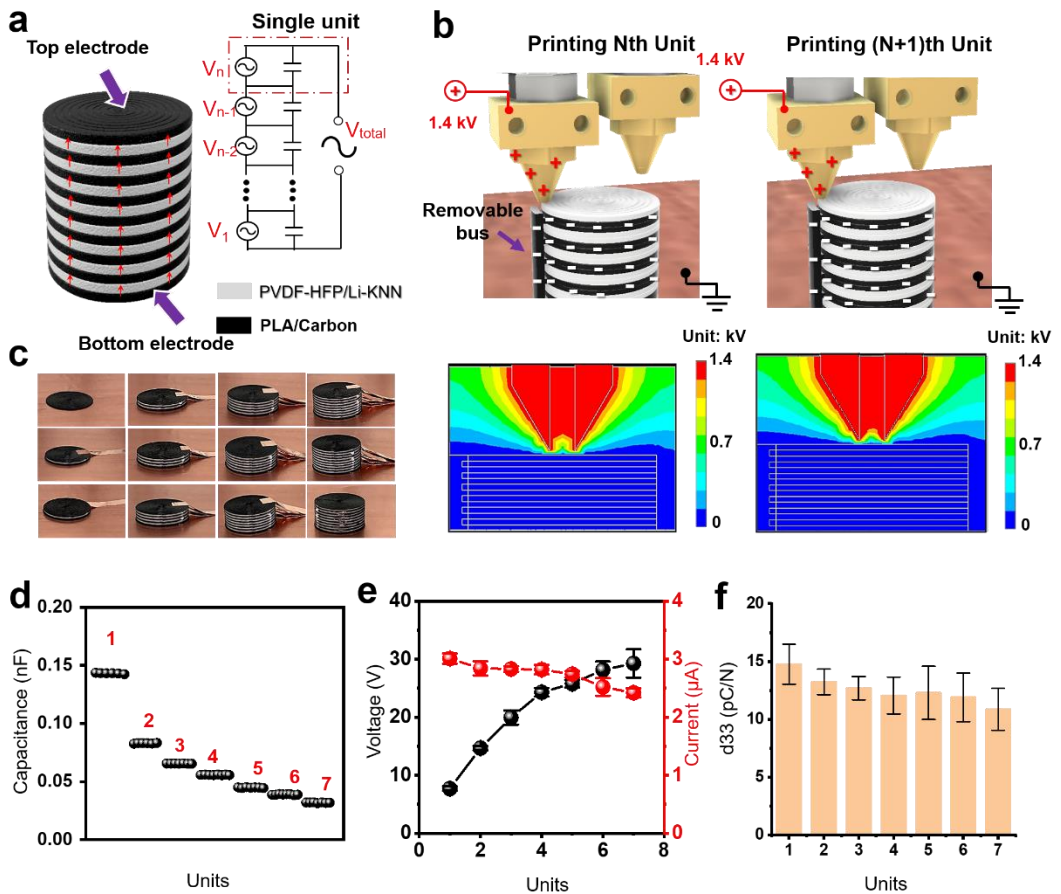


Figure S13. Direct printing *in situ* poled ferroelectric material with in-series connection of all ferroelectric layers. **a**, Schematics of the designated structure with same aligned dipoles and its equivalent circuit. **b**, Electric setup for the consecutive N th unit and $(N+1)$ th unit printing and corresponding potential distribution simulation by a FEA method. The same potential distribution and electric field lead to the same piezoelectricity in each unit. **c**, Detailed printing process by applying a removable copper bus. **d**, The measurement of capacitance of printed structure with varying units from 1 to 7. **e**, Open-circuited voltage and short-circuited current outputs of printed structure with varying units from 1 to 7. **f**, The d_{33} coefficient as a function of printed units.

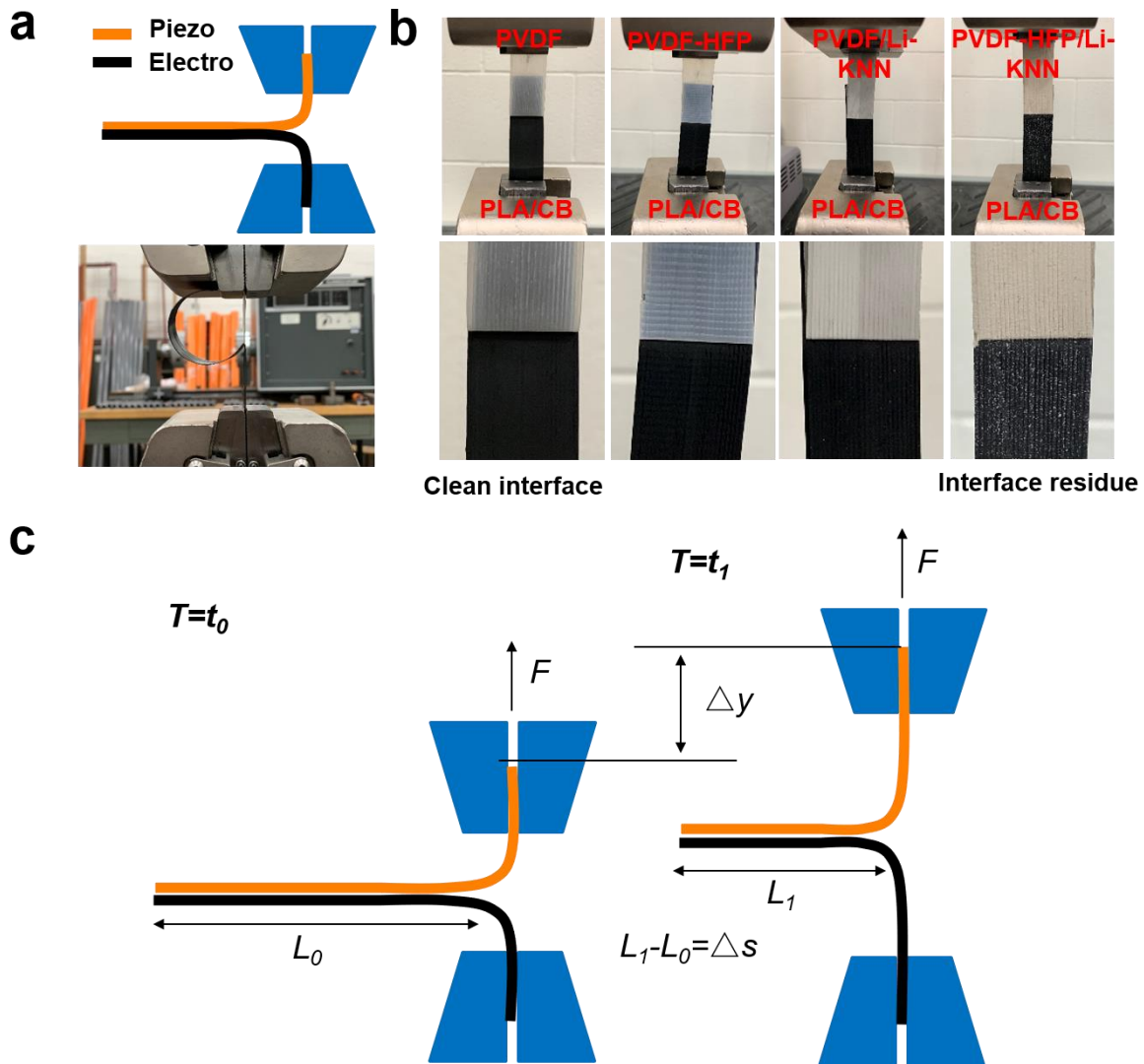


Figure S14. Interfacial adhesion characterization of printed bilayer structures. **a**, Schematic and experimental setup for measuring interface force between printed bilayer structure through a Trouser peel test. By gradually pulling an initial cleft between printed bilayers, the interfacial force could be detected. **b**, Digital images of peeling four different kinds of bilayer films consisting of PLA/CB paired with PVDF, PVDF-HFP, PVDF/Li-KNN, and PVDF-HFP/Li-KNN, respectively. Visible residue was found in the exposed surface of PVDF-HFP/Li-KNN and PLA/CB bilayer in contrast to clean surface from PVDF and PLA/CB bilayer. **c**, Schematics of the Trouser peel test with specific parameters at different time frames.

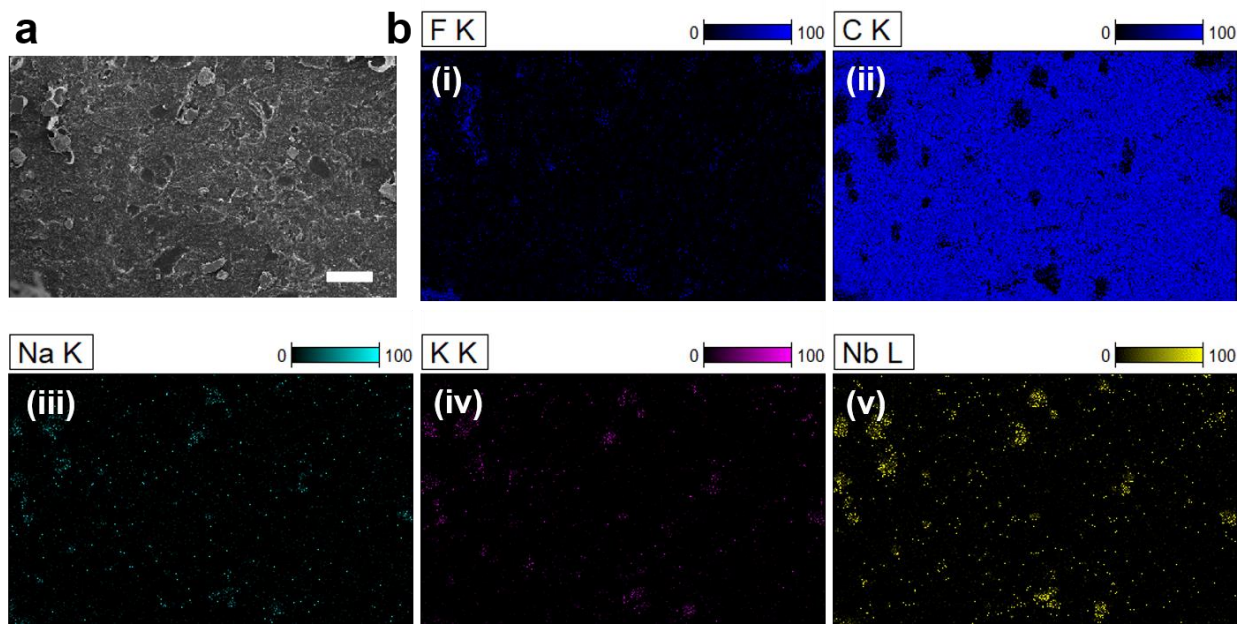


Figure S15. PLA/CB peeling surface observation. **a**, SEM image of the exposed surface of PLA/CB layer from a PVDF-HFP/Li-KNN and PLA/CB bilayer structure. **b**, EDS mapping of F (i), C (ii), Na (iii), K (iv) and Nb (v) elements of the newly exposed surface.

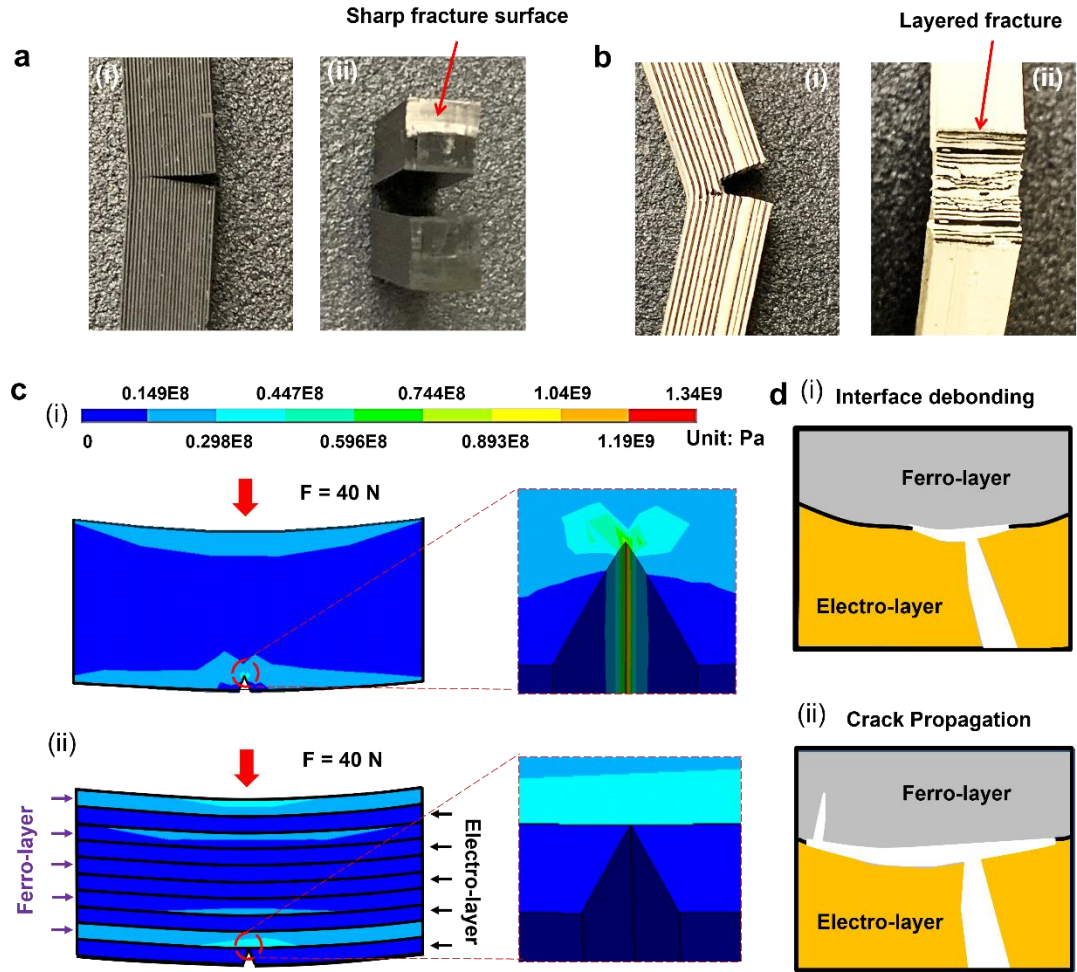


Figure S16. Toughness enhancement and mechanism. **a**, (i) Digital image showing crack propagation path of an as-printed PLA/CB sample. (ii) Digital image showing the fracture surface of the PLA/CB sample. A sharp fracture surface was obtained. **b**, (i) Digital image showing crack propagation path of an as-printed ferroelectric metamaterial sample. (ii) Digital image showing the fracture surface of the ferroelectric metamaterial sample. A layered fracture characteristic was obtained. **c**. FEA simulation of stress distribution in homogenous PLA/CB material (i) and ferroelectric metamaterial consisting of alternative PVDF-HFP/Li-KNN and PLA/CB layers (ii). In the simulation, each layer is 400 μm , and a force of 40 N is applied. The moduli for ferro-layer and electro-layer are 0.4 GPa and 1.6 GPa, respectively. **d**. Crack behavior in soft PVDF-HFP/Li-KNN layer with interface debonding (i) and crack propagation (ii).

Mechanism behind Toughness Enhancement

The driving force J_{tip} at the crack tip can be estimated as:⁸

$$J_{tip} = K^2(1-\nu^2)/E$$

where K is the stress intensity factor, v is the Poisson's ratio, and E is the Young's modulus. The stress intensity factor K is related to the local stress σ of the crack tip:

$$K \propto \sigma\sqrt{\pi a}$$

where π is constant and a is the length of the crack. Since v is close (~ 0.3) for PLA and PVDF composite, the driving force is determined by the local stress and modulus. The FEA simulation of stress distribution revealed that the stress at the crack tip (1.34E9 Pa) of homogeneous electrode material (Figure 16c-i) is more than four times higher than the counterpart (3.3E8 Pa) in soft layer of printed ferroelectric structure (Figure 16c-ii). Given the E of both material (0.4 GPa for ferro-layer and 1.6 GPa for electro-layer), the J_{tip} in electrode material is also more than four times higher than the J_{tip} in soft layer of the ferroelectric metamaterial. As a result of that, the lower driving force in soft layer suppresses the crack propagation and enhances the fracture resistance (toughness). Further increasing the stress causes the debonding of ferro-layer and electro-layer (Figure S16d-i). When the increasing stress is larger than the critical fracture stress (σ_f) in the soft layer, the crack deflects and continues to propagate in the soft layer (Figure S16d-ii).

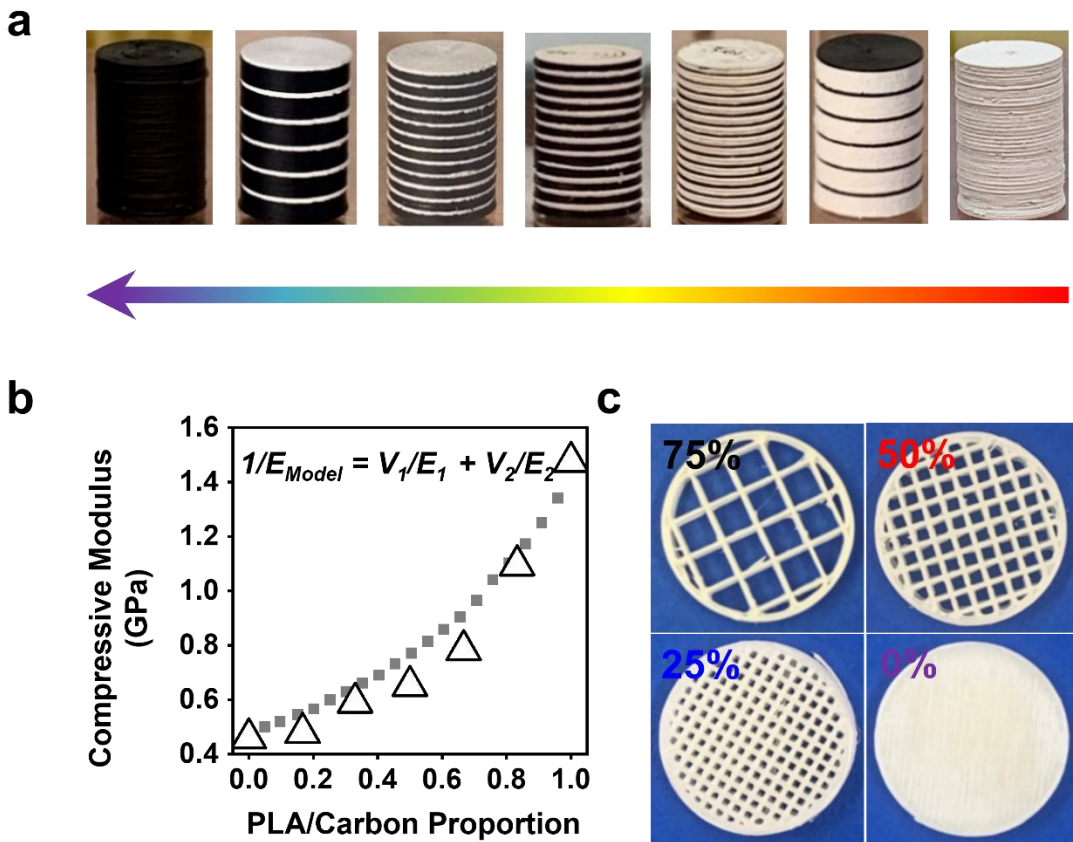


Figure S17. Mechanical modulus tuning. **a**, Digital image of printed structure with varying electrode compositions from 0 to 100 percent. **b**, Corresponding compressive modulus, which could be controlled within the range from 0.57 GPa to 1.48 GPa following the Reuss model. **c**, The digital image of printed structures with different porosity ranging from 0% to 75%.

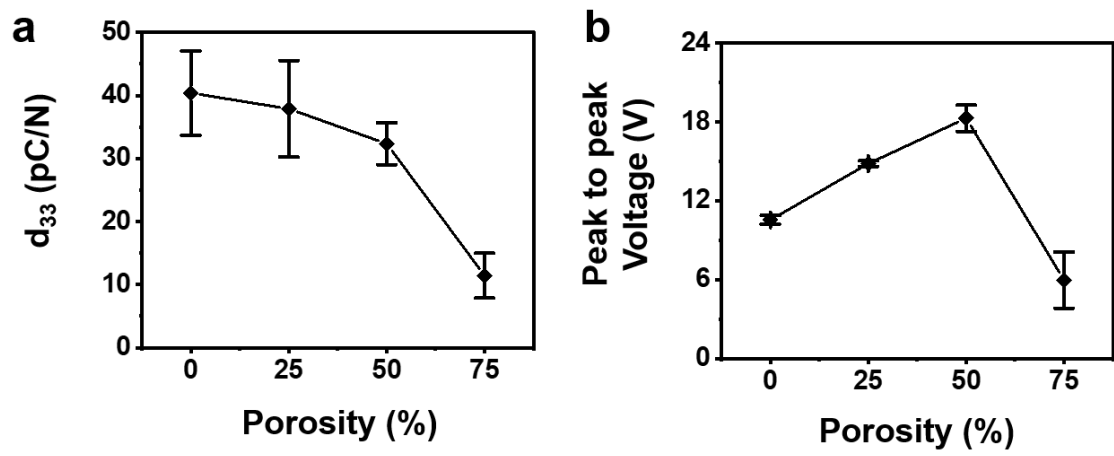


Figure S18. Influence of porosity on piezoelectricity. **a**, The d_{33} of ferroelectric metamaterials as a function of designated porosity. **b**, The peak-to-peak voltage of ferroelectric metamaterials as a function of designated porosity.

Supporting Table

Table S1. Estimated equivalent dielectric constants ϵ_r and piezoelectric voltage constants g_{33} of printed structures.

| Ferroelectric Layers | ϵ_r | g_{33} (mV • m/N) |
|----------------------|--------------|---------------------|
| 1 | 69.06 | 24.21 |
| 2 | 255.78 | 13.06 |
| 3 | 452.98 | 10.09 |
| 4 | 966.85 | 6.31 |
| 5 | 1688.10 | 4.22 |
| 6 | 2327.60 | 3.51 |
| 7 | 3299.57 | 2.81 |

Supporting Movies

Movie S1. Extrusion of ferroelectric composite by a customized extruder system.

Movie S2. Current output of three-unit ferroelectric structure under 100 N mechanical stimuli.

Movie S3. Current output of seven-unit ferroelectric structure under the same mechanical stimuli.

Movie S4. Lighting 10 LED bulbs by 3D printed bulk ferroelectric structure.

Movie S5. Low-voltage-assisted printing of 25-unit scaled ferroelectric structure.

References

1. Cao, J. H.; Zhu, B. K.; Xu, Y. Y., Structure and Ionic Conductivity of Porous Polymer Electrolytes Based on PVDF-HFP Copolymer Membranes. *J. Membr. Sci.* **2006**, *281* (1-2), 446-453.
2. Hietala, S.; Holmberg, S.; Karjalainen, M.; Nasman, J.; Paronen, M.; Serimaa, R.; Sundholm, F.; Vahvaselka, S., Structural Investigation of Radiation Grafted and Sulfonated Poly(vinylidene Fluoride), PVDF, Membranes. *J. Mater. Chem.* **1997**, *7* (5), 721-726.
3. Tofangchi, A.; Han, P.; Izquierdo, J.; Iyengar, A.; Hsu, K., Effect of Ultrasonic Vibration on Interlayer Adhesion in Fused Filament Fabrication 3D Printed ABS. *Polymers* **2019**, *11* (2), 315.
4. Kendall, K., Thin-Film Peeling - Elastic Term. *J. Phys. D: Appl. Phys.* **1975**, *8* (13), 1449-1452.
5. Munch, E.; Launey, M. E.; Alsem, D. H.; Saiz, E.; Tomsia, A. P.; Ritchie, R. O., Tough, Bio-Inspired Hybrid Materials. *Science* **2008**, *322* (5907), 1516-1520.
6. Yang, Y.; Li, X. J.; Chu, M.; Sun, H. F.; Jin, J.; Yu, K. H.; Wang, Q. M.; Zhou, Q. F.; Chen, Y., Electrically Assisted 3D Printing of Nacre-Inspired Structures with Self-Sensing Capability. *Sci. Adv.* **2019**, *5* (4), eaau9490.
7. Bower, A. F., Modeling Material Failure. *Applied Mechanics of Solids*. 1 ed.; CRC press: Boca Raton, 2009; pp 547-613.
8. Fischer, F. D.; Kolednik, O.; Predan, J.; Razi, H.; Fratzl, P., Crack Driving Force in Twisted Plywood Structures. *Acta Biomater.* **2017**, *55*, 349-359.